Research Square

Preprints are preliminary reports that have not undergone peer review. They should not be considered conclusive, used to inform clinical practice, or referenced by the media as validated information.

Carbon Support–Alkali Interplay Controls CO_2 Slip during Direct Air Capture and Methanation over Dual-Functional Materials

Enrique Garcia-Bordejé

jegarcia@icb.csic.es

Instituto de Carboquímica (ICB-CSIC) https://orcid.org/0000-0001-8158-1270

Victor Bordejé

Instituto de Carboquímica (ICB-CSIC)

María Morales

University of distance Education (UNED)

Antonio Guerrero-Ruíz

UNED

Inmaculada Rodríguez-Ramos

Instituto de Catálisis y Petroleoquímica (ICP-CSIC)

José María Conesa

Instituto de Catálisis y Petroleoquímica https://orcid.org/0000-0001-5470-7958

Article

Keywords: direct air capture (DAC), integrated methanation, dual functional material (DFM), alkali metals, ruthenium catalyst

Posted Date: October 15th, 2026

DOI: https://doi.org/10.21203/rs.3.rs-11152786/v1

License: This work is licensed under a Creative Commons Attribution 4.0 International License. Read Full License

Additional Declarations: There is **NO** Competing Interest.

Carbon Support–Alkali Interplay Controls CO_2 Slip during Direct Air Capture and Methanation over Dual-Functional Materials

Victor Bordejé[a], José María Conesa[b], María V. Morales[c], Antonio Guerrero-Ruiz[c,d], Inmaculada Rodríguez-Ramos[b,d], Enrique García-Bordejé[a],

[a] Instituto de Carboquímica (ICB-CSIC), Miguel Luesma Castán 4, E-50018 Zaragoza, Spain,

[b] Instituto de Catálisis y Petroleoquímica (CSIC), 28049, Madrid, Spain

[c] Departamento de Química Inorgánica y Química Técnica, UNED, 28040, Madrid, Spain

[d] Grupo de Diseño y Aplicación de Catalizadores Heterogéneos, Unidad Asociada UNED-CSIC (ICP), Spain

Abstract

Dual-functional materials (DFMs) combine CO_2 capture from diluted sources with catalytic conversion to fuel. However, the contribution of the alkali phase is difficult to separate from that of reactive oxide supports. Here, Ru-Na and Ru-K DFMs were prepared on two carbon supports with different pore structures: mesoporous high-surface-area graphite (HSAG) and predominantly microporous activated carbon (AC). The materials were evaluated in cycles of CO_2 capture from humid air at 40 °C followed by methanation in 20% H_2/Ar during heating to 300 °C.

Activated-carbon-supported DFMs showed higher CO_2 capture capacities than their HSAG-supported counterparts. The use of a chemically inert carbon support enabled the clear assessment of intrinsic role of the alkali metal. Alkali identity determined how efficiently the captured carbon was used: Ru-Na retained the captured species within the methanation temperature window and achieved nearly complete conversion to CH_4 with negligible CO_2 slip across the investigated loading range, whereas Ru-K released substantial CO_2 at higher loadings. RuNa(1:10) on AC maintained stable performance over 25 cycles after an initial conditioning period. Reducing the Ru content from 3 wt%

Corresponding author: Tel.:+ 34 976733977; fax.: +34 976733318 *E-mail address:* jegarcia@icb.csic.es

to 1.5 wt% preserved negligible CO_2 slip but decreased capture capacity by about 20%. These results show that DFM optimisation requires matching the stability and reactivity of the captured species with the catalytic methanation window rather than simply maximising CO_2 uptake.

Keywords: direct air capture (DAC); integrated methanation; dual functional material (DFM); alkali metals; ruthenium catalyst

1. Introduction

CO_2 capture and utilisation (CCU) or storage (CCS) are important routes for managing emissions and supporting a circular carbon economy [1,2]. Aqueous amines are widely used to capture CO_2 from flue gas, but their use involves corrosion, toxicity, water consumption and energy-intensive regeneration. Solid sorbents can reduce some of these limitations. Chemisorbents are particularly suitable for dilute CO_2 streams such as air (about 0.04 vol%) because they provide more selective adsorption even in the presence of humidity [3]. Amines immobilized in solid sorbents have also been proposed but they have stability issues because decompose at moderate temperature[4]. In contrast, supported alkali compounds are attractive because they are inexpensive, non-corrosive and thermally stable. However, alkali phases[5,6] can react with oxide supports. For example, K-containing mixed phases can form on Al_2O_3 or MgO and hinder regeneration [5–8]. Basic oxide supports may also capture CO_2 themselves [9,10]. Carbon supports have therefore been investigated as a way to limit alkali-support reactions for DAC [11,12], and hydrophobic carbon surfaces can favour carbonation over competing hydration reactions [12,13].

Conventional capture produces a CO_2-rich stream that must be compressed, transported and either stored or converted. Integrating capture and conversion in one process can reduce these additional steps. This process, termed reactive capture [14–16], can be carried out using dual-functional materials (DFMs) that combine a sorbent phase with a catalytic phase. The proximity between the two functions may favour synergistic effects such as enhanced heat and mass transport, integration of conversion/regeneration, and intensification of the process. DFMs have been studied for CO_2 concentrations ranging from flue gas [8,17–23] to air [19,24–29]. The capture phase is commonly an alkali

compound, while a transition metal catalyses conversion to CO or CH_4. Direct air capture is usually performed near ambient temperature to avoid heating large volumes of air, followed by a temperature increase for conversion. During this temperature swing, CO_2 can desorb before the catalyst becomes active, causing CO_2 slip [30]. Alkali identity affects capture capacity, carbonation kinetics, regeneration and cyclic stability[9–12,31], but these effects are difficult to separate from support-CO_2 and support-alkali interactions in oxide-supported materials [5,7,8].

Most DFMs for direct air capture use porous oxide supports such as alumina. These supports can form mixed phases with the alkali component and can also adsorb CO_2 on surface hydroxyl groups which is desorbed at low temperature [25,26,32,33]. Carbon supports provide a useful comparison because their contribution to CO_2 chemisorption is expected to be smaller, although this must be verified experimentally. There are limited instances of their application as supports for DFMs in DAC processes, such as carbon nanofibers [34,35] or high surface area graphite [31].Carbon-supported DFMs have been reported on carbon nanofibers. Ru-K/carbon nanofiber materials remained stable for 20 cycles of DAC and methanation [34]. In our previous work[31], Ru-Cs/HSAG combined high CO_2 capture with stable cycling, whereas aggregation of the Ba promoter in Ru-Ba/HSAG reduced the utilization of capture phase. These studies indicated that both alkali identity and the dispersion of the capture phase affect capture and conversion.

In this work, we compare Ru-Na and Ru-K DFMs supported on mesoporous high surface area graphite (HSAG) and predominantly microporous activated carbon (AC) for de DAC and conversion. Alkali loading was varied at a constant Ru loading to determine how alkali loading, support porosity and alkali identity affect CO_2 capture, methanation and CO_2 slip. The best-performing composition was tested over 25 cycles, and the effect of Ru loading and impregnation sequence were examined. Finally, this DFM was benchmarked against those reported for direct air capture.

2. Experimental

2.1. *Synthesis of dual-functional materials*

High-surface-area graphite (TIMREX HSAG 300, Imerys) and Norit SX Ultra Cat activated carbon (Cabot) were used as supports. The metals were added by successive incipient-wetness impregnation, first with the alkali precursor and then with the Ru precursor. The Ru loading was fixed at 3 wt% relative to the mass of carbon, and alkali-

to-Ru molar ratios from 2.5 to 14.6 were prepared. The required amount of KNO_3 or $NaNO_3$ (Merck) was dissolved in a 4:1 water/ethanol mixture at the volume needed to fill the support pores. After impregnation, the powder was dried at room temperature for 12 h and treated in N_2 at 300 °C for 1 h using a heating rate of 1 °C min^{-1}. Ru was then added by incipient-wetness impregnation using ruthenium nitrosyl nitrate (Johnson Matthey). The material was dried for 12 h, treated in N_2 at 300 °C for 1 h and reduced in H_2 under the same temperature programme before testing.

2.2.*Material characterisation*

N_2 adsorption-desorption isotherms were measured at 77 K using a Micromeritics ASAP 2020 after outgassing the samples at 473 K for 4 h. The BET surface area was calculated over a relative-pressure range of 0.05-0.30. Total pore volume was estimated from the amount adsorbed at a relative pressure of 0.99. Pore-size distributions were calculated applying the DFT model. Micropore surface area was determined by the t-plot method, and mesopore surface area was obtained by subtracting the micropore area from the BET area.

Temperature-programmed surface reaction (TPSR) experiments were performed in a Micromeritics AutoChem II. The DFMs were reduced at 300 °C, cooled and exposed at 40 °C either to simulated air containing 400 ppm CO_2 or to 5% O_2/Ar. Air-exposed samples were heated to 110 °C in Ar to remove water, cooled to room temperature and then heated to 300 °C in 10% H_2/Ar at 10 °C min^{-1}. To distinguish the contributions from carbonation and oxidation, the sample was subsequently cooled to 40 °C in Ar, treated with 5% O_2/Ar and subjected to a second TPSR experiment.

Crystalline phases were examined by X-ray diffraction (XRD) using a PANalytical X′Pert Pro powder diffractometer in Bragg-Brentano geometry with Cu Kα radiation (λ = 0.1544 nm, 45 kV and 40 mA). Patterns were recorded from 4° to 90° 2θ with a step size of 0.04°. Before XRD analysis, the DFMs were reduced in H_2 (30 mL min^{-1}) at 300 °C for 1 h and subjected to the DAC step.

X-ray photoelectron spectra were acquired using an ESCAPlus Omicron instrument for HSAG supported DFMs or a custom SPECS analyser assembled from Omicron hardware and equipped with a SPECS HSA 3500 analyser and SpecsLab Prodigy software for Norit-supported DFMs. Both systems used Mg Kα radiation. The energy scale was

calibrated against Ag $3d_{5/2}$ at 368.27 eV. Measurements were performed under ultrahigh vacuum (<10^{-10} Torr), and binding energies were referenced to the C 1s signal at 284.6 eV. Spectra were fitted in CasaXPS using a Shirley background and GL(70) line shapes; the full width at half maximum was constrained to a maximum of 2 eV.

High-resolution transmission electron microscopy (HRTEM) images were acquired using a JEOL JEM-GRANDARM 300cF microscope with a cold field-emission gun operated at 300 kV. Reduced samples were ground, dispersed ultrasonically in ethanol and deposited on carbon-coated Cu grids. Mean Ru particle diameters and standard deviations were calculated from at least 200 particles using $d_p = \Sigma n_i d_i / \Sigma n_i$. Local elemental analyses were obtained by energy-dispersive X-ray spectroscopy (EDS) using a JEOL Centurio silicon drift detector and a nominal spot size of 1 nm.

2.3. Cyclic CO_2 capture and methanation tests

CO_2 capture and regeneration experiments were performed with 50 mg of DFM (<100 µm) mixed with SiC and placed in the centre of a vertical quartz reactor with a 6 mm outer diameter. A thermocouple positioned in the bed was connected to a Eurotherm temperature controller, and gas flow rates were controlled with Bronkhorst mass-flow controllers. Before each test, the DFM was reduced in H_2 (60 mL min^{-1}) at 300 °C for 1 h using a heating rate of 10 °C min^{-1}. During capture, 60 mL min^{-1} (STP) simulated air containing 400 ppm CO_2 and 21% O_2 in Ar was fed up to the breakthrough curve reached 380-400 ppm (30 min for most samples) while the reactor was held at 40 °C. Humid air was generated by passing the feed through water maintained at 30 °C. After CO_2 breakthrough, the reactor was purged first with Ar for 30 min and then with 20% H_2/Ar,for 15 min both at 60 mL min^{-1}, to remove physisorbed or weakly retained CO_2 and H_2O. Regeneration was performed in 20% H_2/Ar while heating to 200, 250 or 300 °C. Outlet gases were analysed with a Pfeiffer mass spectrometer by monitoring m/z = 2 (H_2), 15 (CH_4), 18 (H_2O), 28 (CO), 40 (Ar) and 44 (CO_2). Signals were corrected against the Ar baseline. CO_2 and CH_4 concentrations were obtained by calibration of m/z = 44 and 15, respectively. The CO contribution was calculated from m/z = 28 after subtracting the CO_2 contribution. Calibration was checked independently using an Arnel Clarus 690 gas chromatograph.

The CO_2 capture capacity, expressed in mmol $g^{-1}$of DFM was calculated by integrating the CO_2 breakthrough curve:

$$CO_2\ capacity = \frac{F_{air}}{m_{DFM}} \int (CO_{2\ \mathrm{in}} - CO_{2\ out})\ dt \qquad eq.\ 1$$

where *F_air* is the molar flow rate of simulated air at STP, m_DFM is the DFM mass, $CO_{2,in}$ and $CO_{2,out}$ are the inlet and outlet CO_2 concentrations, and t is time. Blank experiments with a SiC bed were used to correct the breakthrough curves for the response time of the experimental system.

3. Results and discussion

3.1. Characterisation of dual functional materials

3.1.1. N_2 physisorption

The two carbon supports have distinct pore structures, as shown by their N_2 adsorption–desorption isotherms (Figure 1). HSAG displays a type IV isotherm, typical of a mesoporous material, with a BET surface area of 298 $m^2\ g^{-1}$ and a total pore volume of 0.41 $cm^3\ g^{-1}$. In contrast, the Norit activated carbon displays a mixed type I/type IV isotherm, consistent with a microporous network that also contains mesopores. It has a higher BET surface area (935 $m^2\ g^{-1}$) and total pore volume (0.77 $cm^3\ g^{-1}$). Micropores account for 8% of the total pore volume of HSAG and 31% of that of Norit AC.

Several loadings of K (Figure 1 and Table 1) and Na (Figure S1 and Table S1 of supplementary material) were deposited on both supports. Surface areas and pore volumes were normalized to the support mass. Both quantities decreased as the alkali metal content increased for the RuK and RuNa series on both supports. For RuK/H samples, the main decrease occurred in the 2-20 nm mesopore range (Figure 1b), and the RuK (1:10)/H retained only 65% of the original mesopore volume. The reduction in mesopore volume is not attributable to a surface coating of the pores, which would result in pores with narrower diameters, but rather due to the complete filling of these mesopores. Therefore, K carbonate or oxide particles of sizes around 2-20 nm are expected in RuK/H samples. For RuK/N samples, the largest decrease occurred in micropore volume, so that RuK(1:10)/N retained 95% of the original mesopore volume (Figure 1d and Table 1) . These results indicate preferential pore occupation or blocking of some pores by alkali. Although it is not a direct measurement of alkali-particle size, it suggests that K oxides or carbonates are confined to smaller pores on Norit (<2 nm) than on HSAG (2-20 nm). Similar conclusions can be derived from the textural properties of RuNa series (Figure S1 and Table S1).

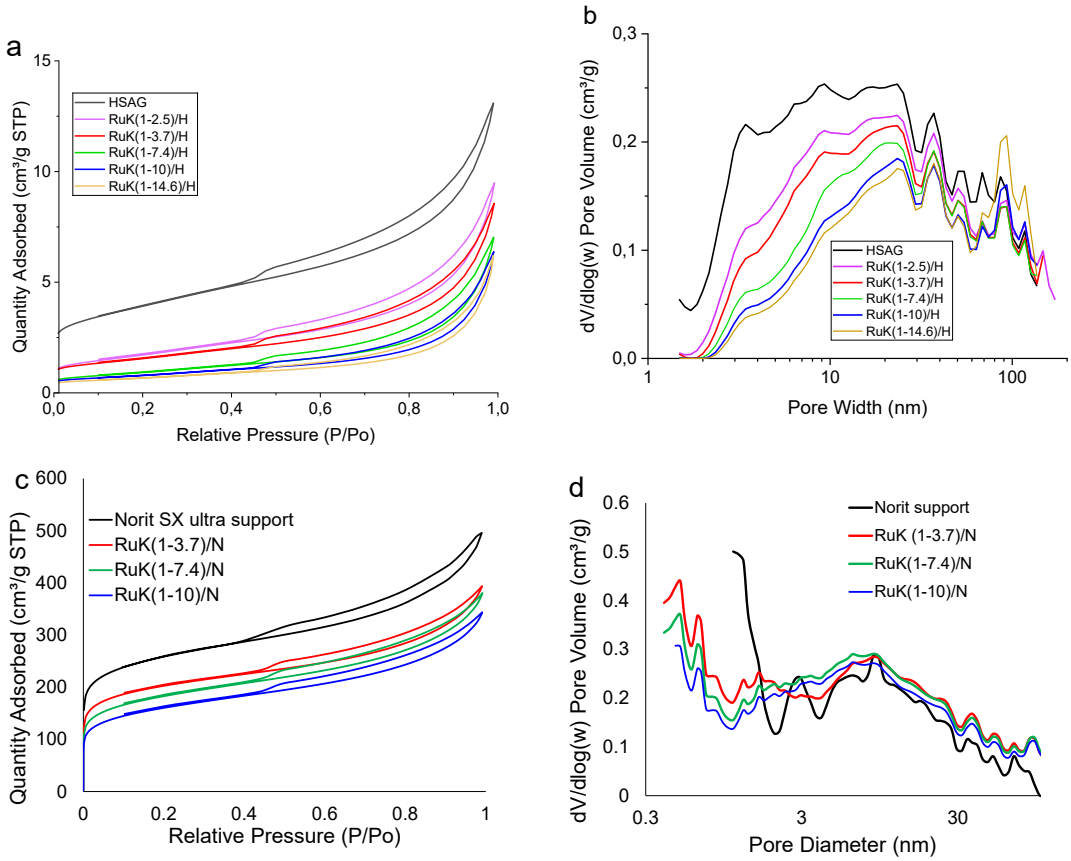

Figure 1. N_2 adsorption-desorption isotherms (left panels, a and c) and pore-size distribution calculated by DFT model (right panels, b and d) for RuK DFMs with different K loadings: (a,b) HSAG-supported materials and the bare HSAG support; (c,d) AC(Norit)-supported materials and the bare AC support.

Table 1. Textural properties of RuK DFMs supported on HSAG and AC normalised to the support mass.

Sample	Surface area	Pore Volume	Micropore Surface Area* (S_{mic})	Micr. Pore vol. *	Mesop Surface Area (S_{mes})	Meso Pore vol.	Percentage of support weight
	m^2g^{-1}	$cm^3\ g^{-1}$	$m^2\ g^{-1}$	$cm^3\ g^{-1}$	$m^2\ g^{-1}$	$cm^3\ g^{-1}$	%

HSAG	298	0,41	n.d.	n.d.	298	0,41	100
RuK(1:2.5)/H	145	0,35	n.d.	n.d.	145	0,35	94,4
RuK(1:3.7)/H	131	0,31	n.d.	n.d.	131	0,31	93,2
RuK(1:7.4)/H	83	0,27	n.d.	n.d.	83	0,27	89,6
RuK(1:10)/H	72	0,25	n.d.	n.d.	72	0,25	87,3
RuK(1:14.6)/H	63	0,25	n.d.	n.d.	63	0,25	83,4
Norit AC	935	0.77	615	0.24	320	0.53	100
RuK(1:3.7)/N	780	0,65	492	0,19	288	0,46	93,2
RuK(1:7.4)/N	723	0,65	402	0,16	321	0,49	89,6
RuK(1:10)/N	652	0,61	343	0,13	309	0,48	87,3

* calculated from the N_2 adsorption isotherm using the t-plot method
n.d.: not reliably determined by the t-plot method

3.1.2. X-ray diffraction

Figure 2 shows the XRD patterns of the DFMs after reduction and DAC step. HSAG-supported materials (Figure 2a,b) display the reflections of hexagonal graphite (PDF 01-0646) at 26.4º, 42.8º, 44.6º, 54.4º and 77.4º of the support (HSAG300). In contrast, Norit-supported materials (Figure 2c,d) show broad features from disordered carbon and weak reflections assigned to SiO_2 impurities in the support. The SiO_2 impurity was inert in the reactions involved in this study. No reflections assigned to Ru (38.4°, 42.0° and 44.7°) or RuO_2 (28.1°, 35.0° and 54.4°) were detected. This result indicates that crystalline Ru-containing domains were below the XRD detection limit (4 nm).

At the lowest alkali loadings, the XRD patterns closely resembled those of the carbon supports, indicating that the alkali-containing phases were poorly crystalline or highly dispersed. Weak additional reflections appeared at higher loadings and increased in intensity with alkali content, particularly for RuK. In the K-containing DFMs, these reflections were assigned to K_2CO_3 (PDF 87-0730) and $KHCO_3$ (PDF 70-1167). In the Na-containing DFMs, they were tentatively assigned to Na_2O (PDF 02-1285), Na_2CO_3 (PDF 37-0451) and trona, $Na_2CO_3 \cdot NaHCO_3 \cdot 2H_2O$ (PDF 78-1064). The increasing intensity is consistent with the formation of larger and/or more crystalline alkali-rich domains at high loading. The weaker reflections of the Na-containing DFMs indicate

either lower crystallinity or higher dispersion than in the corresponding K-containing samples.

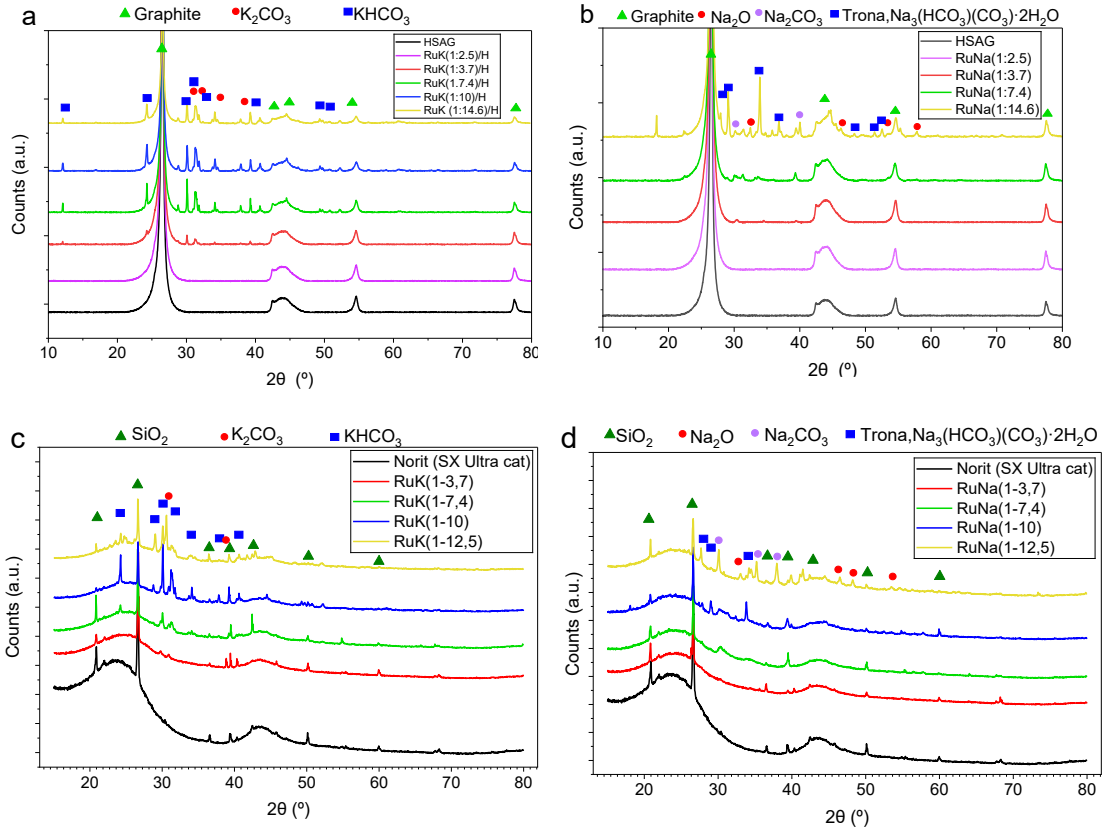

Figure 2. XRD patterns of DFMs after CO_2 capture from air at room temperature: (a) RuK/HSAG; (b) RuNa/HSAG; (c) RuK/AC; (d) RuNa/AC.

3.1.3. Transmission electron microscopy (TEM)

The Ru morphology and dispersion, and the spatial distribution of the alkali phase were investigated by high-resolution transmission electron microscopy (HRTEM), scanning transmission electron microscopy in high-angle annular dark-field mode (STEM-HAADF) and energy-dispersive X-ray spectroscopy (STEM-EDS). Figure 3 presents the results obtained for RuNa(1:10)/H DFM, and Figures S2-S5 show those for other representative DFMs. Na and K cannot be resolved reliably by HRTEM because of their low atomic number and limited contrast against carbon. Conversely, Ru provides sufficient contrast for structural analysis.

Ru nanoparticles were well dispersed and showed lattice fringes consistent with metallic Ru (Figure 3a). Some particles also displayed spacings compatible with RuO_2, probably

because of surface oxidation during air exposure. RuNa(1:10)/H had a mean Ru diameter of 1.7 nm (Figure 3b). Across the samples examined, mean diameters ranged from 1.3 to 1.7 nm (Figures S2 and S3). The distributions broadened slightly at high alkali loading, particularly on HSAG, but the mean Ru size remained similar. STEM-EDS maps showed Ru and the alkali elements distributed uniformly over the same support regions, with no large alkali-rich domains in the areas examined (Figure 3c and Figures S4 and S5).

Because the mean Ru particle size varied only slightly across the examined samples, Ru size alone is unlikely to explain the differences in capture and methanation discussed below. Alkali speciation, size and proximity to Ru should contribute to the different behaviour, but the present microscopy study is not able to quantify these effects.

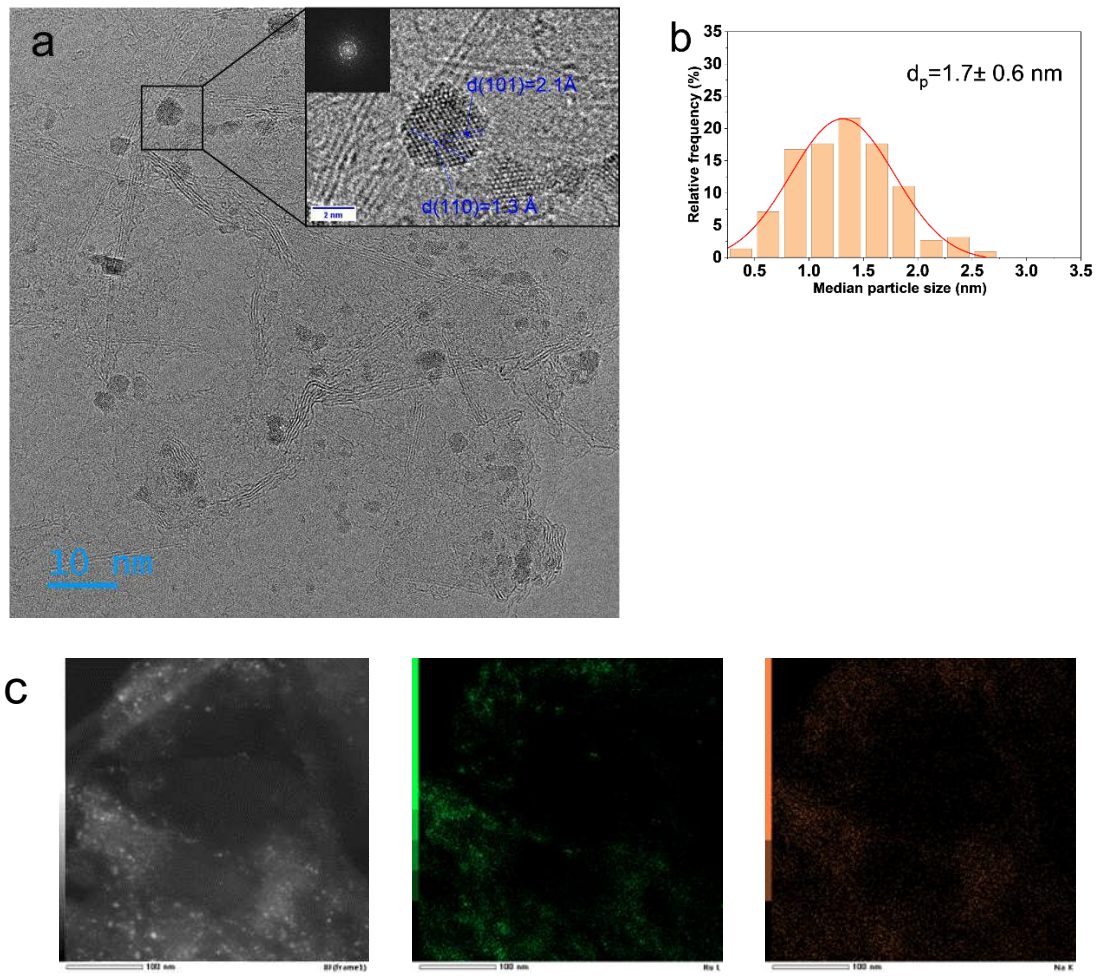

Figure 3. Characterisation of RuNa(1:10)/H: (a) HRTEM image with a magnified Ru nanoparticle and its FFT; (b) Ru particle-size distribution; and (c) STEM image and EDS maps of Ru (green) and Na (orange).

3.1.4. Temperature programmed surface reaction

Figure 4 compares H_2 consumption during TPSR experiments for AC-supported DFMs exposed at 40 °C either to simulated air containing 400 ppm CO_2 (solid lines) or to 5% O_2/Ar (dashed lines) after a previous reduction at 300 °C. Therefore, for the continuous line TPSR, the DFM was both oxidised and carbonated at 40ºC whereas, for the discontinuous line, the DFM was exclusively oxidised at 40ºC. This allows decoupling the contributions of carbonation and oxidation. The O_2-treated samples show a low-temperature peak assigned to reduction of reoxidised Ru. This peak occurs near 110 °C for RuNa and 120 °C for RuK and shifts slightly to higher temperature as alkali loading increases. Therefore, the surface oxidation of Ru is more pronounced in the presence of K compared to Na, and is further enhanced with a higher loading of alkaline metal. A weak feature near 250 °C may arise from either oxidised alkali species or oxygen-containing surface groups on the carbon support. Relative to the O_2-treated sample, the air-exposed DFM shows a shoulder at 120-150 °C, particularly for RuK, which is consistent with reaction of bicarbonate-derived species. A broader high-temperature peak appears at 200-225 °C for RuNa and above 280 °C for RuK. This peak shifted to higher temperatures as the alkali loading increased and it is associated with hydrogenation of carbonate-derived species and concomitant CH_4 formation.

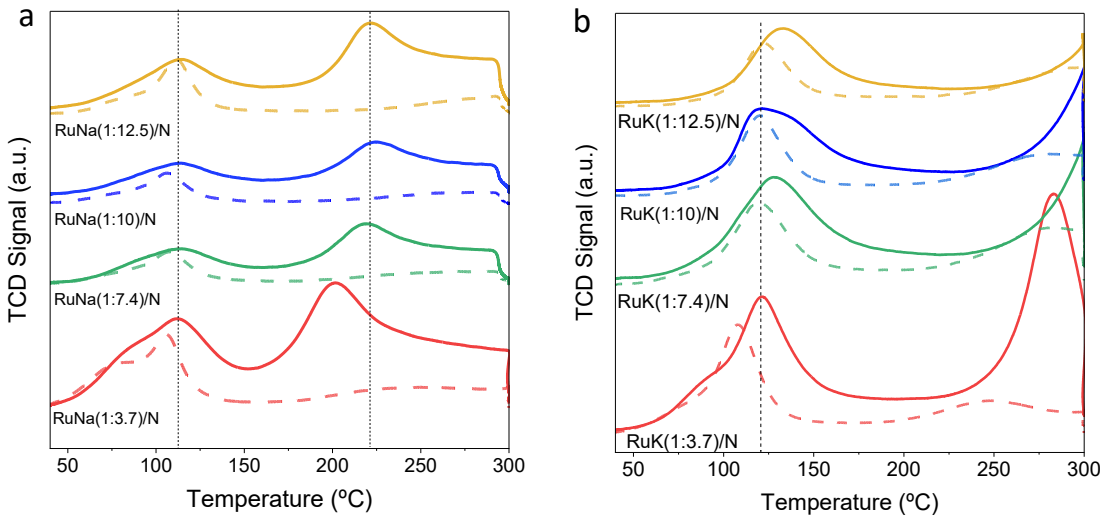

Figure 4. TPSR profiles of (a) RuNa/N and (b) RuK/N with different alkali loadings. Solid lines correspond to samples reduced at 300 °C and exposed to simulated air containing 400 ppm CO_2 at 40 °C. Dashed lines correspond to reduced samples treated with 5% O_2/Ar at 40 °C.

3.1.5. XPS

The Na 1s spectra were fitted with components centred at 1071.6 and[36][36] 1073.1 eV, assigned to carbonate/bicarbonate [36] and oxide/hydroxide environments [37,38], respectively (Figure 5 a, b). A third component near 1075 eV appeared[39] only at the highest loadings. This component cannot be assigned to a specific Na phase because this binding energy is not commonly reported for Na 1s and the carbon-supported samples may undergo differential charging. For instance, Na 1s peak at 1075 eV was only found for Na^+ in a highly insulating and electron-withdrawing microenvironment of a fluoride materials[39]. The relative contribution of Na carbonates with respect to oxidized Na decreases with the loading. This could indicate the presence of larger Na oxide particles as loading increases. In larger Na particles, carbonation is likely restricted to the surface, leaving the core as sodium oxide due to the hindered diffusion of CO_2.

The fitting of O 1s peak is more ambiguous because the overlapping of oxygen from oxygenated groups of carbon with inorganic oxygen from alkali metal oxides and carbonates. Nevertheless, we performed the fitting of O 1s and assigned the peaks according to the literature (Figure S6 of supplementary material). We have made the following observations that have to be treated with caution because the ambiguity of the fitting. The relative contribution of C-O and COOH with respect to C=O increased with loading, particularly for the AC support. As alkali loading increases, we also observed an increased intensity of chemisorbed water (more hydrophilic) and of the Na KLL Auger peak at 536.5 eV. The Na KLL feature in the O 1s region confirms the proximity of Na and O [40]. Therefore, while the XPS spectra show clear alkali-loading dependent trends that suggest changes in the material, the interpretation of these changes remains inconclusive.

Ru 3p spectra were fitted according to the procedure reported in [41] (Figure S7). At the lowest alkali loading, HSAG-supported DFMs showed a larger metallic-Ru contribution than the corresponding AC-supported samples. Increasing alkali loading decreased the metallic-Ru contribution on HSAG until it became comparable with that on AC. TEM showed similar mean Ru particle sizes at low and high loadings, so the XPS trend cannot be attributed directly to Ru particle size. Differences in surface oxidation, local chemical environment or charging may contribute, but the present data do not distinguish among these effects. One hypothesis may be a decrease of electron density donation from Na to Ru as loading increases due either to more oxidised Na species or to larger Na particles with lower interphase with the support.

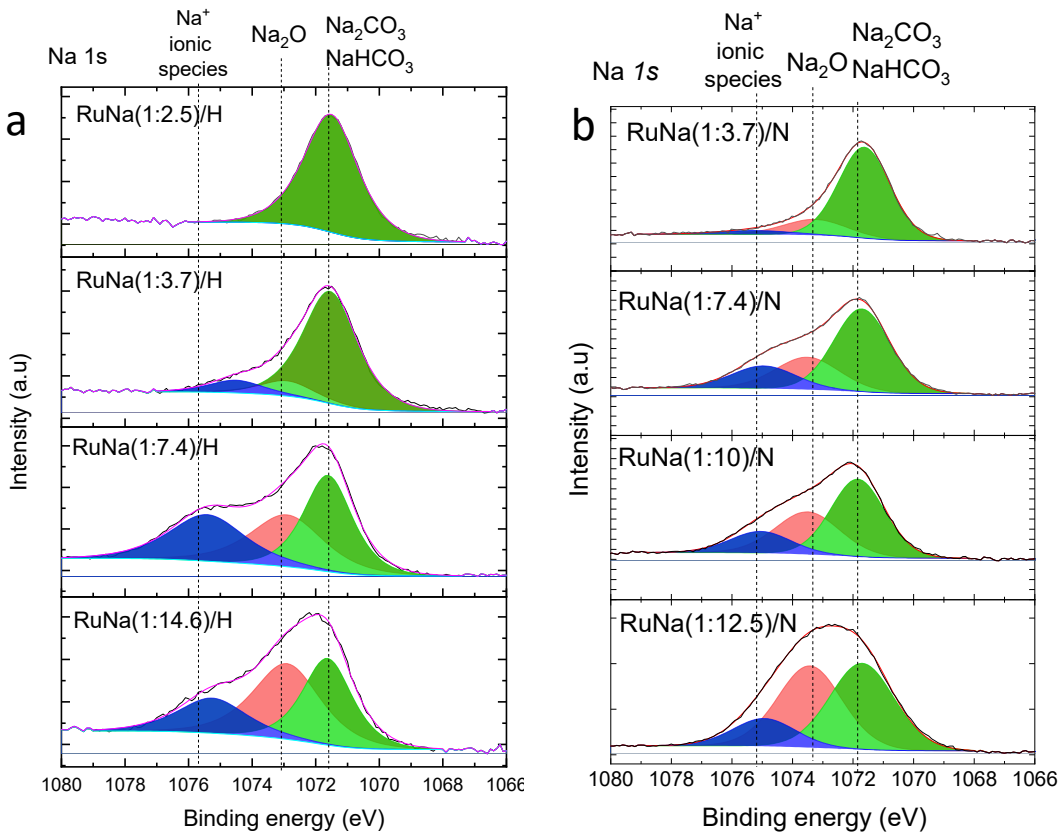

Figure 5. Fitting of Na *1s* XPS peaks of RuNa DFMs with different alkali loadings on the two supports: (a) Na 1s peak for HSAG-supported DFM; (b) Na 1s peak for AC-supported DFM.

3.2. Cyclic CO_2 capture and methanation

3.2.1. Effect of regeneration temperature and air humidity

The effect of regeneration temperature was examined for RuNa(1:2.5)/H and RuK(1:2.5)/H by heating in 20% H_2/Ar to 200, 250 or 300 °C and holding for 30 min (Figure 6). CH_4 and CO_2 outlet profiles are shown as solid and dashed lines, respectively. CH_4 onset temperatures, apparent initial production rates and total yields were calculated from these profiles (Table S2). The onset temperatures were similar for RuNa and RuK, but RuK gave a sharper peak and a higher apparent rate at 250 and 300 °C. RuNa produced a broader profile that reached a plateau near 250 °C, which is maintained until the dwell temperature is reached. Upon reaching this target temperature, the CH_4 concentration decayed during the constant temperature period. Regeneration at 200 °C gave substantially less CH_4, indicating incomplete regeneration. Heating to 300 °C increased the total CH_4 yield, particularly for RuNa, and was therefore selected for the subsequent experiments.

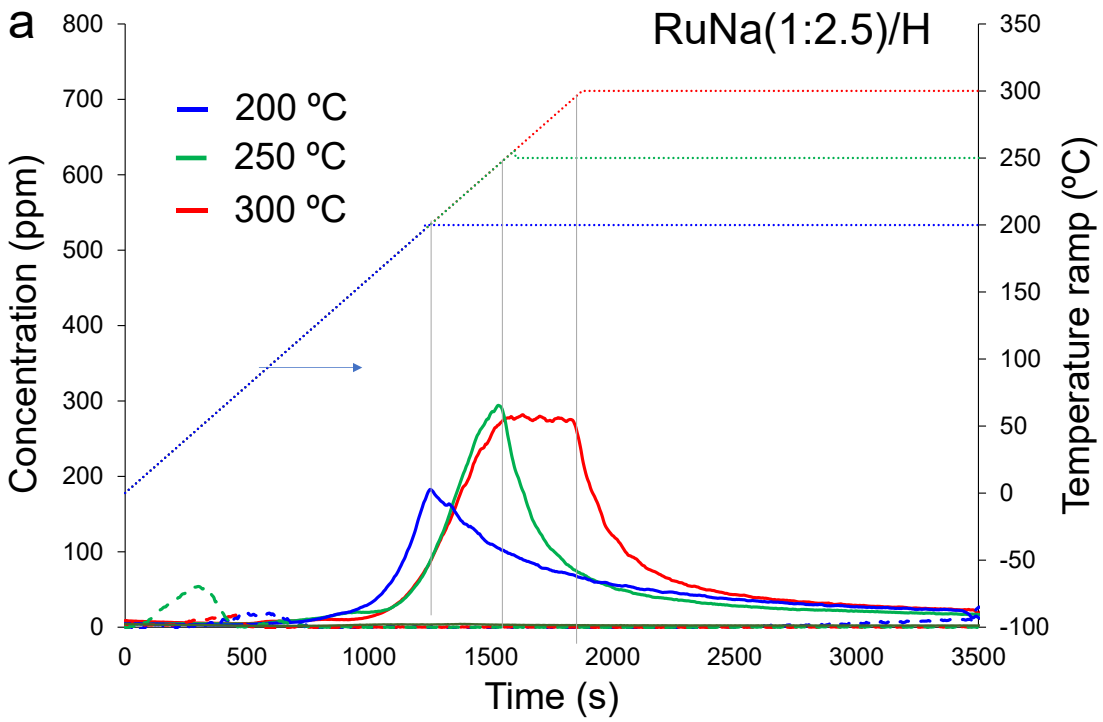

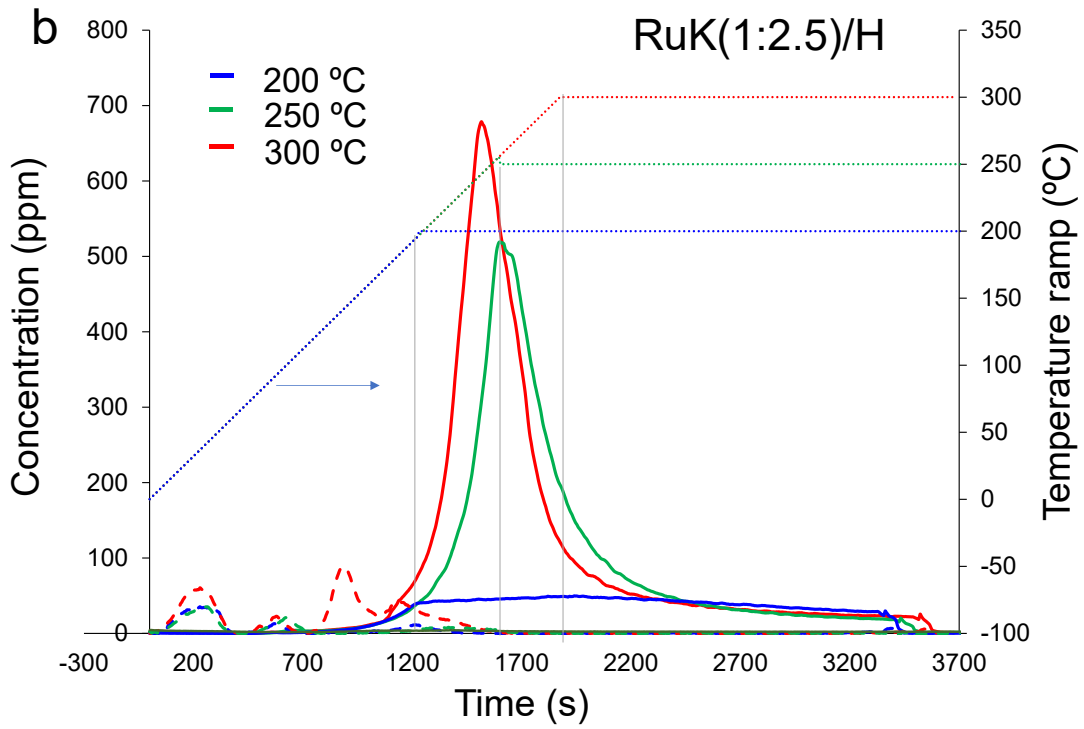

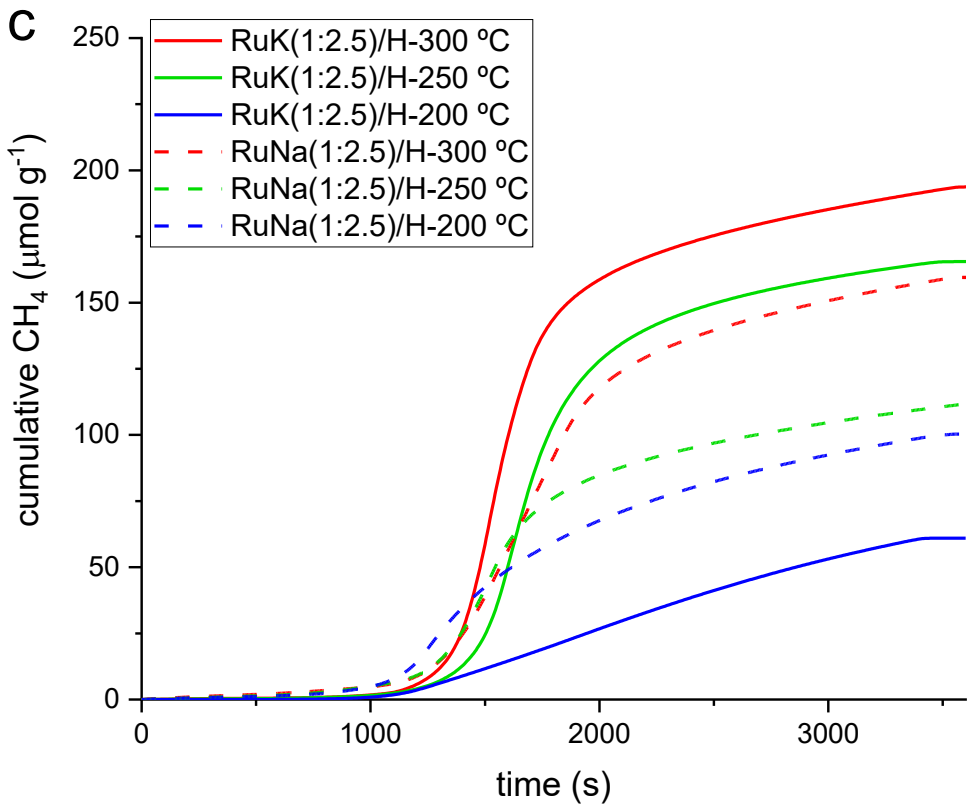

Figure 6. CH_4 and CO_2 outlet profiles during regeneration of (a) RuNa(1:2.5)/H and (b) RuK(1:2.5)/H to different final temperatures. Solid lines show CH_4 and dashed lines show

CO_2. (c) Cumulative CH_4 yield calculated from panels (a) and (b). CO_2 was captured from humid air at 40 °C.

The effect of humidity was assessed with RuNa/H samples of different Na loadings (Figure 7). Capture from humid air systematically resulted in slightly higher CO_2 uptake and negligible CO_2 release during regeneration. After capture from dry air, a significant fraction of CO_2 desorbed below 100 °C, before CH_4 formation began (Figure 7b). After humid-air capture, CO_2 remained on the DFM until the temperature approached the CH_4 onset near 180 °C and was then converted to CH_4 (Figure 7b).

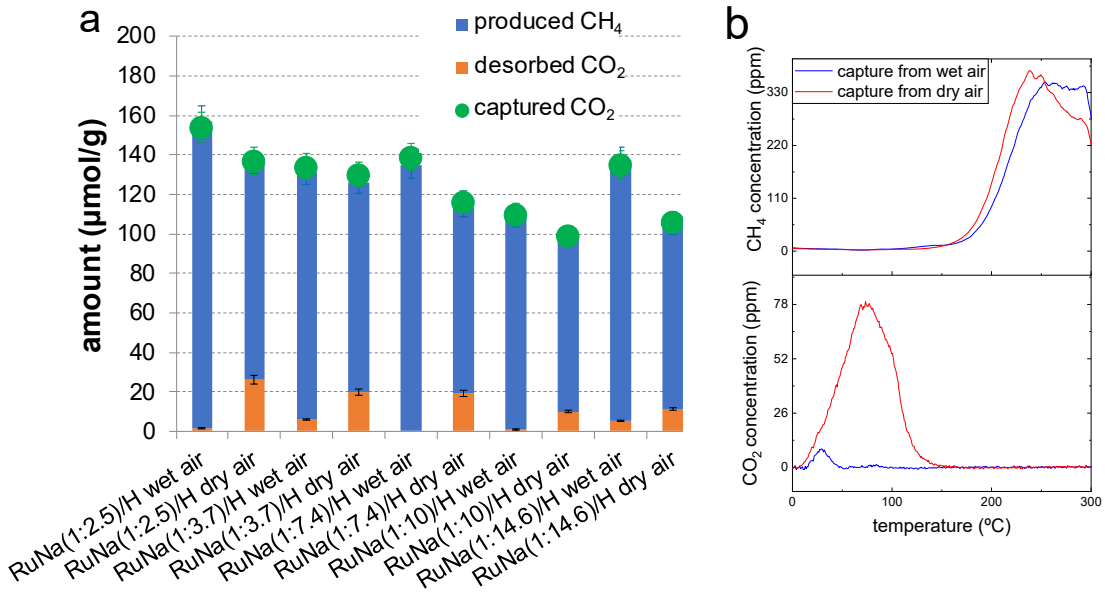

Figure 7. Comparison between capture from humid and dry air. (a) carbon balances for RuNa/H samples with different Na loadings; (b) CH_4 and CO_2 profile during regeneration of RuNa (1:2.5)/H.

Humidity therefore plays the dual role of slightly increasing capture capacity and changing the retention or speciation of the captured CO_2. Under dry conditions, part of the CO_2 is weakly adsorbed and desorbs below the methanation onset. Under humid conditions, the captured carbon remains retained until hydrogenation over Ru becomes kinetically significant. Water thus improves not only the CO_2 uptake but, more importantly, the overlap between CO_2 release and catalytic conversion. This study does not address the identification of the surface species, which will be the objective of future works.

3.2.2. Comparison of HSAG and activated carbon supports

Figure 8 compares carbon balances for RuNa and RuK on HSAG and Norit AC. Na loading has little effect on CO_2 uptake for RuNa/H series, whereas for RuNa/N series uptake increased up to RuNa(1:10)/N and then levels off (Figure 8c). RuK showed a similar loading effect: capture increased up to RuK(1:12.5)/N on Norit AC, but only up to RuK(1:7.4)/H on HSAG and then levels off. The sub-proportional increase in CO_2 uptake with alkali loading indicates that a decreasing fraction of the added alkali remains accessible for CO_2 capture. The decreasing fraction of accessible alkali would agree with an increasing alkali particle size. Although the characterisation techniques did not allow to determine the exact alkali particle size, there are some indirect evidences of an increasing alkali size such as the appearance of crystalline alkali-containing phases by XRD, the progressive pore filling/blocking observed by N_2 physisorption, and the increasing contribution of non-carbonated/oxidised Na species detected by XPS. AC-supported DFMs reached higher maximum CO_2 uptakes than their HSAG-supported counterparts, approximately 800 μmol g^{-1} for RuK/N and 400 μmol g^{-1} for RuNa/N, respectively. This could be also tentatively explained by a smaller alkali size on AC than on HSAG, which would agree with a confinement effect within the micropores.

At comparable loading, RuK generally captured more CO_2 than RuNa. However, alkali identity had the opposite effect on CO_2 utilisation. RuNa released negligible CO_2 during regeneration and converted almost all captured carbon to CH_4. In contrast, RuK showed little CO_2 slip only at the lowest loadings and, at higher K loadings, 30-50% of the captured carbon was released as CO_2.

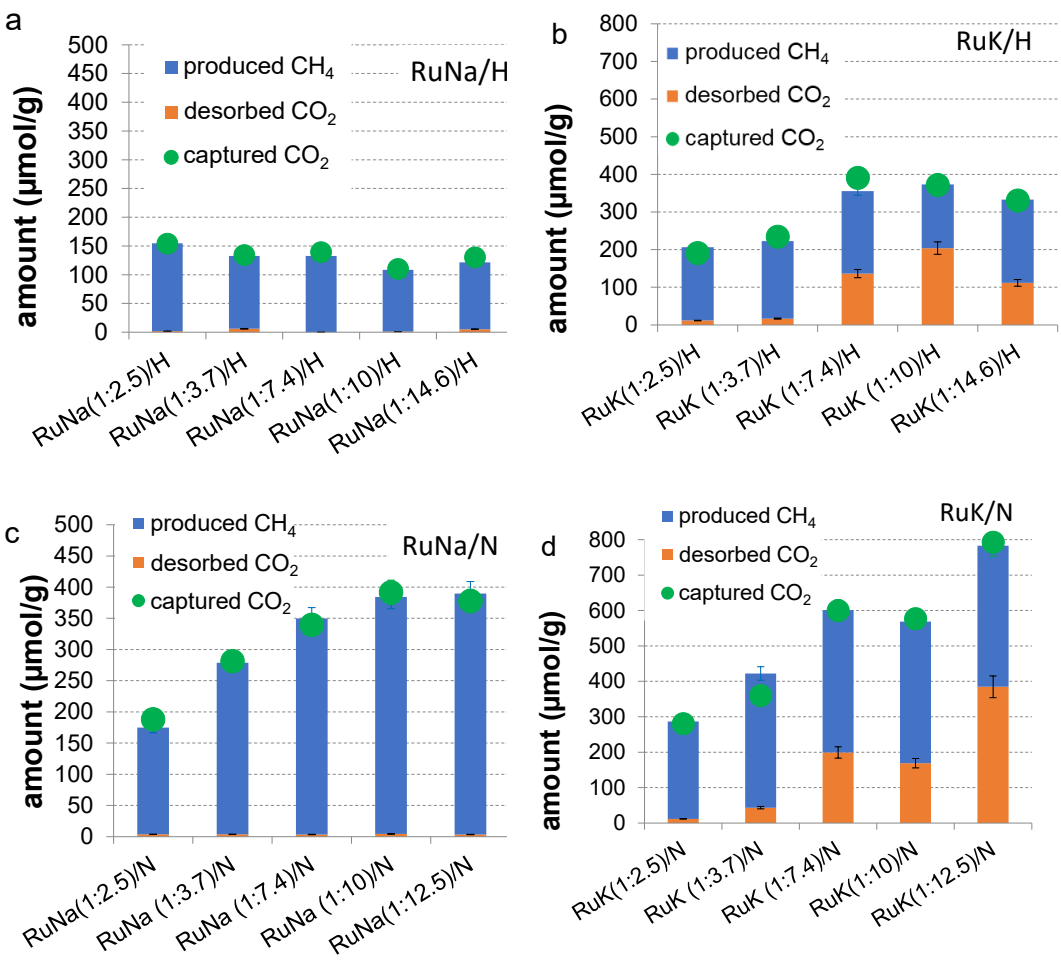

Figure 8. Carbon balances showing captured CO_2, produced CH_4 and released CO_2 for the different alkali loadings: (a) RuNa/HSAG; (b) RuK/HSAG; (c) RuNa/Norit AC; (d) RuK/Norit AC. Note that the vertical scales differ between right and left panels. The error bar corresponds to standard deviation of 5 cycles.

Figures 9 and 10 show the CH_4 and CO_2 outlet profiles during regeneration for HSAG- and AC-supported DFMs, respectively. Cumulative CH_4 yields, onset temperatures and apparent initial rates are reported in Tables S3 and S4. RuK on both supports (Figures 9c and 10c) released CO_2 near 150 °C and formed CH_4 at higher temperatures, whereas RuNa released negligible CO_2. The CH_4 onset and peak temperatures were generally higher for RuK (Tables S3 and S4), indicating that K addition inhibits the methanation reaction to a greater extent than Na. The apparent initial rates were sometimes higher for RuK because its CH_4 peak occurred later in the temperature ramp and was sharper. Two observations are particularly noteworthy across all the dataset. The lowest-loading HSAG samples showed lower onset temperatures, while the highest K loadings on both supports showed

lower apparent initial rates. Norit-supported samples generally gave significantly higher initial rate and narrower CH_4 profiles than HSAG-supported samples. This would agree with a different alkali metal size proposed above. The comparison of initial rates is somehow ambiguous because they reflect not only the intrinsic reactivity of the catalyst but also with diffusional control, which would prevail for larger alkali metal particles or longer distance between the capture and catalytic sites. Because the mean Ru particle size remained similar across the series, these differences are more likely related to the chemical environment and accessibility of the capture phase rather than to changes in Ru dispersion.

Compared with the alumina-supported RuNa materials reported previously [32], the carbon-supported RuNa series maintained low CO_2 slip over a wider range of Na loadings. This behaviour is consistent with a negligible contribution from support-derived CO_2 as demonstrated by bare-support control experiments. Accordingly, carbon support is a convenient support for uncoupling the intrinsic thermal-dependent behaviour of different alkali metals from the effect of the support on the capture and methanation. The RuNa results indicate that most captured carbon remains retained until a temperature at which methanation kinetics becomes relevant. RuK, by contrast, appears[32] to form a broader distribution of retained species: a weakly bound fraction is released before methanation, while another fraction reacts only at higher temperature. This temperature mismatch explains how RuK combine high capture capacity with lower overall conversion efficiency.

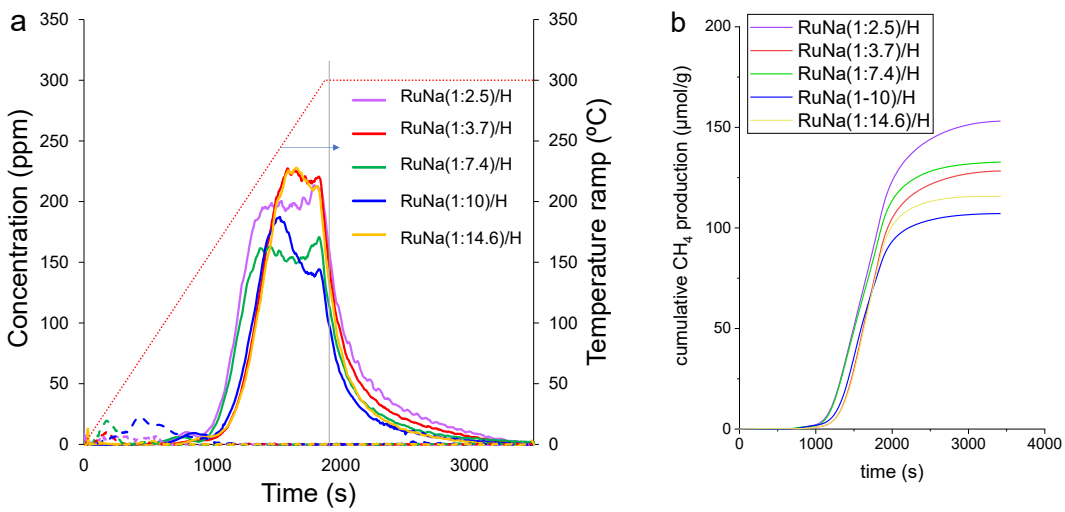

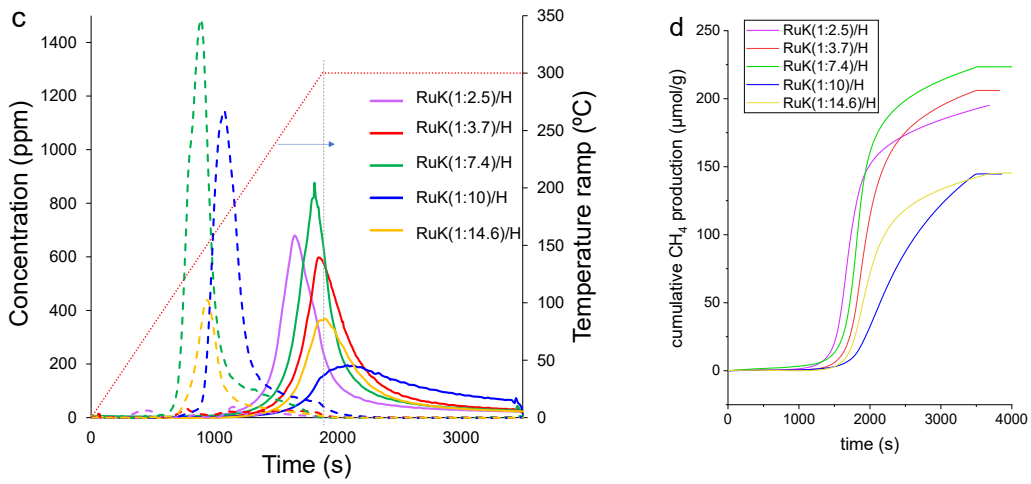

Figure 9. Regeneration of HSAG-supported DFMs. Left panels: CO_2 (dashed line) and CH_4 (solid line) outlet profiles for (a) RuNa/H and (c) RuK/H. Right panels: cumulative CH_4 yield for (b) RuNa/H and (d) RuK/H calculated from profiles in left panels.

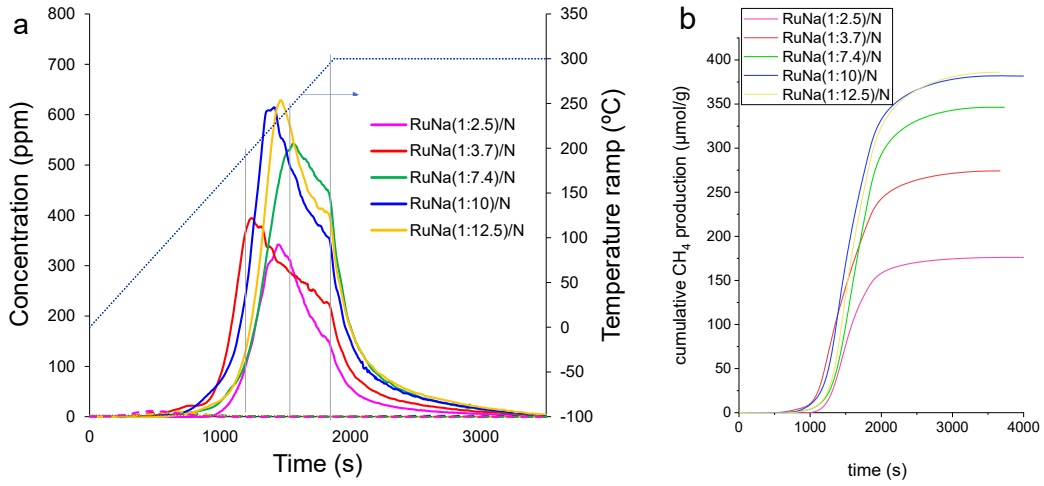

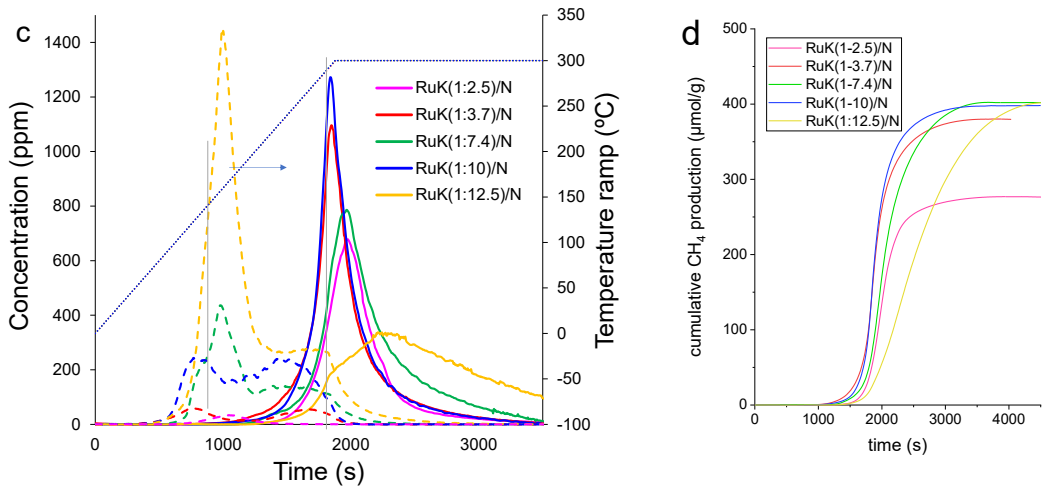

Figure 10. Regeneration of Norit AC-supported DFMs. Left panels: CO_2 (dashed line) and CH_4 (solid line) outlet profiles for (a) RuNa/N and (c) RuK/N. Right panels: cumulative CH_4 yield for (b) RuNa/N and (d) RuK/N calculated from profiles in left panels.

3.2.3. Optimisation and cyclic stability

RuNa(1:10)/N was selected for cyclic testing because it combined high capture capacity with negligible CO_2 slip (Figure 8c). The material was tested over 25 capture-methanation cycles (Figure 11). In the first cycle, the measured CH_4 yield exceeded the CO_2 captured in the preceding step, indicating a contribution from labile carbon or residual carbon-containing species in the fresh material. The carbon balance approached closure after the first three conditioning cycles. From cycle 4 onwards, the capture capacity remained close to 380 µmol g^{-1} and the conversion of captured CO_2 remained close to 100%. These results demonstrate stable performance over the 25 cycles tested.

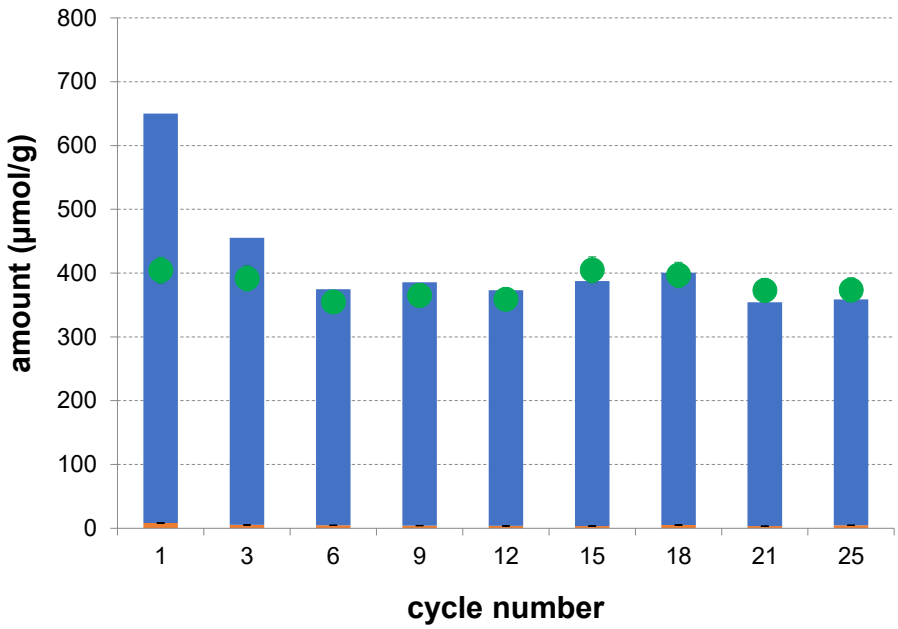

Figure 11. Captured CO_2, CH_4 yield and released CO_2 for selected cycles during the 25-cycle test of RuNa(1:10)/N.

Reversing the impregnation sequence, by adding Ru before Na, slightly decreased performance (Figure 12a). The original impregnation sequence was therefore retained. To reduce Ru use, samples containing 0.5, 1.5, 2.3 or 3 wt% Ru were prepared at a constant Na content of 6.8 wt%. CO_2 uptake increased with Ru loading up to 2.3 wt% and was similar at 2.3 and 3 wt% (Figure 12a and Table 2). Therefore, a higher amount of Ru contributes to a higher CO_2 uptake probably because a more complete regeneration of the capture sites. Moreover, increasing Ru loading shifted the CH_4 onset and peak to lower temperatures (Figure 12b and Table 2), indicating the enhanced hydrogenation as Ru loading increased. The 0.5 wt% Ru sample showed the lowest apparent CH_4 rate and the highest CO_2 slip (Figure 12b and c). The increase of CH_4 production kinetics as Ru loading increases agrees with recent reports [42]. A Ru loading of 2.3 wt% gave performance comparable with 3 wt%, [42] 1.5 wt% maintained negligible CO_2 slip with an approximately 20% lower capture capacity. Reducing Ru to 0.5 wt% impaired both capture and carbon utilisation.

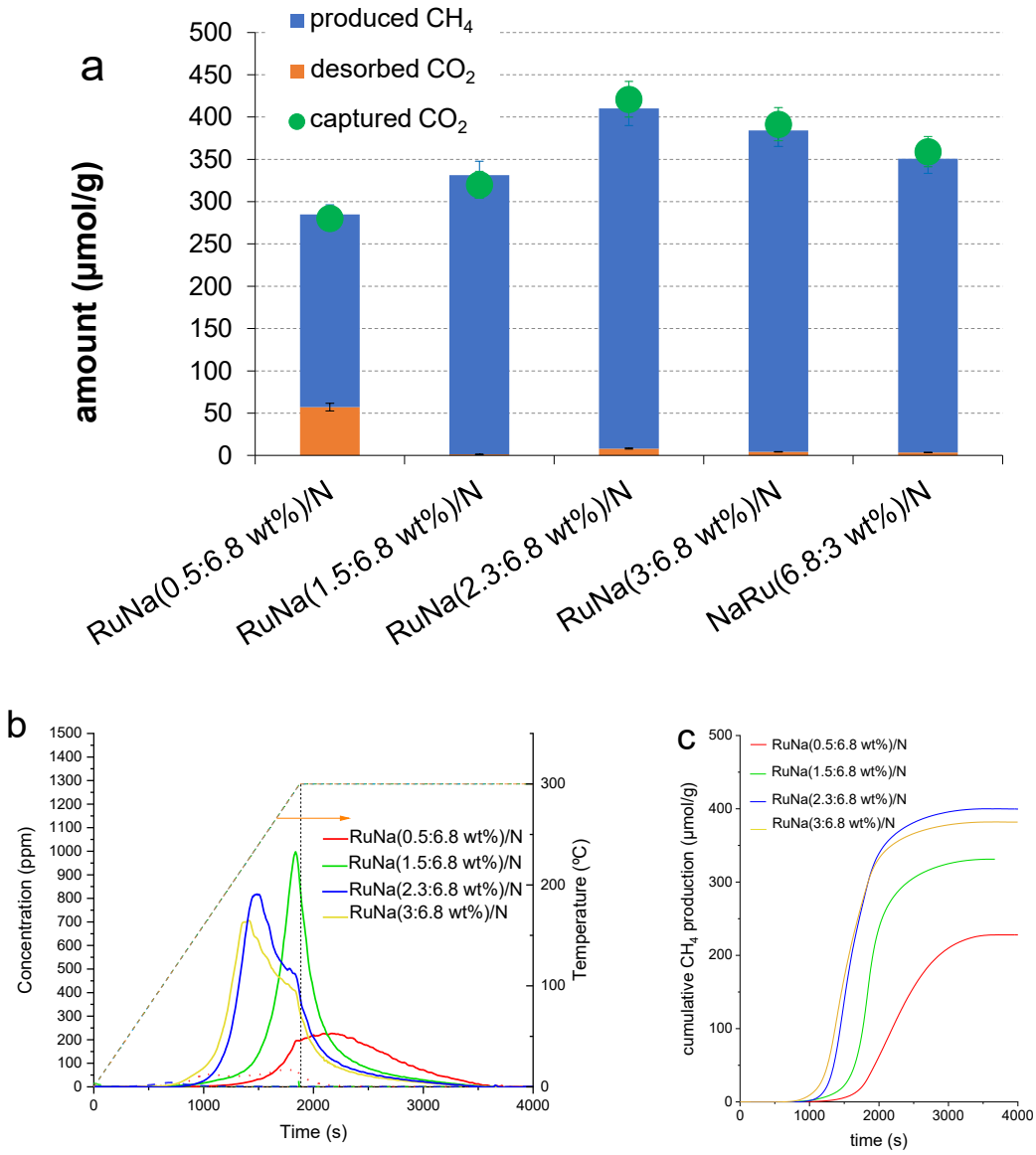

Figure 12. Effect of Ru loading at a constant Na content of 6.8 wt% on RuNa/N performance. (a) Carbon balance after capture and regeneration; the reverse-impregnation sample NaRu(6.8:3 wt%)/N is included for comparison. The error bars correspond to the standard deviation of 5 cycles (b) CH_4 and CO_2 outlet profiles and temperature programme during regeneration of samples containing 0.5-3 wt% Ru. (c) Cumulative CH_4 yield calculated from panel (b).

Table 2. CH_4 onset and peak temperatures, apparent initial CH_4 production rate and total CH_4 yield for RuNa/N with 6.8 wt% Na and different Ru loadings.

DFM	CH_4 peak onset °C	CH_4 peak maximum °C	Initial CH_4 rate µmol g^{-1} s^{-1}	Total CH_4 yield µmol g^{-1}
RuNa (0.5:6.8 wt%)/N	254	300	0.19	228±12
RuNa (1.5:6.8 wt%)/N	206	294	0.71	331±16
RuNa (2.3:6.8 wt%)/N	179	238	0.60	399±20
RuNa (3:6.8 wt%)/N	155	224	0.51	382±19

3.2.4. Benchmarking against reported DFMs for DAC

Reported DFMs for direct air capture can be grouped into two categories: (i) systems operating under isothermal conditions, where CO_2 capture and conversion occur at the same elevated temperature (Table S5) [28,29,43], and (ii) systems operating under dynamic temperature conditions, where CO_2 is captured at near ambient temperature and subsequently heated and converted at elevated temperature (Table S6) [15,19,24–27,30–32,34,35,44–49]. The isothermal studies in Table S5 operated at 320-400 °C. Reported CO_2 uptakes were generally 100-200 µmol g^{-1}. Isothermal operation avoids CO_2 release during a heating ramp, generally leading to lower CO_2 slip than dynamic conditions. However, it requires heating enormous volumes of air in the capture step due to the high dilution of CO_2. In principle, this indicates that the dynamic operation would be less energy consuming but it should be assessed at process level. Dynamic operation avoids heating the air during capture step and the heat is supplied during regeneration step, which is a shorter step. The uptake values compiled in Table S6 are often higher than those in Table S5, although the studies use different humidity, pressure, capture time, mass basis and cycle number. Dynamic operation commonly produces substantial CO_2 slip during heating. Values above 20% were reported in many studies [24–27,30,32,34,35,44–47,49]. Few studies reported a low CO_2 slip [15,19,31,48] along with the present work. In reference [15], a DFM consisting of 1 wt% Ru + ~20 wt% Na on FAU zeolite achieved a CO_2 uptake of 281 µmol g^{-1} with negligible CO_2 slip. The authors claimed that the CO_2 slip was eliminated because CO_2 was strongly adsorbed on Na, whereas Ru was reduced and became active at a lower temperature (~115°C) than the CO_2 desorption temperature

(>150°C). In reference [19], the negligible CO_2 slip could be attributed to the effect of pressure (at 0.9 MPa), which favours the Sabatier reaction and inhibits CO_2 desorption. However, the reported CO_2 uptake was relatively low (168 µmol g^{-1}) in comparison to other DFMs. The last example of negligible CO_2 slip in Table S6 was an unsupported DFM (10 wt% NiCa9Zr) [48], which provided an exceptionally high CO_2 uptake of 7420 µmol g^{-1}. However, this DFM requires a higher temperature for regeneration (450ºC) and its cyclic stability was demonstrated for only five cycles. These systems differ substantially in pressure and regeneration temperature, so uptake alone is not an adequate performance metric.

Both our previous Ru-Ba/HSAG[31] and the present Ru-Na/Norit material showed negligible CO_2 slip under dynamic conditions. Among the DFMs reported exhibiting low CO_2 slip in Table S6, the present material combines one of the highest CO_2 uptake (380 µmol g^{-1}) with stable performance over 25 cycles. Our previous Ru-Na/Al_2O_3 material reached a higher uptake of 740 µmol g^{-1} and 96% conversion at an optimised Na loading [32], but its CO_2 slip was more sensitive to Na loading and capture duration. The main advantage observed here is therefore not the highest absolute uptake, but a wider Na-loading range over which CO_2 slip remains low.

Conclusions

Ru-Na and Ru-K DFMs supported on Norit AC showed higher CO_2 capture capacities than the corresponding HSAG-supported materials. Capture increased with alkali loading on Norit AC but changed little at high loadings on HSAG. N_2 physisorption, XRD and XPS indicated increasing pore occupation and crystallinity and decreasing utilisation of alkali-containing phases with loading.

Alkali identity controlled how efficiently the captured carbon was converted. RuNa exhibited negligible CO_2 slip and nearly complete conversion to CH_4 across the investigated loading range. RuK captured more CO_2 at comparable loading but released 30-50% of the captured CO_2 at high K loadings. The regeneration profiles indicated that RuK contains both weakly retained species, which are released before methanation becomes fast, and species that react only at higher temperature. In contrast, weakly

captured species are absent in RuNa. Efficient DFM design therefore requires matching the temperature windows of stability of the captured species and the catalytic methanation. After the first three conditioning cycles, RuNa(1:10)/N maintained a capture capacity close to 380 μmol g^{-1} and nearly complete conversion during the 25 cycles tested. The Ru loading could be reduced to 2.3 wt% with performance comparable to 3 wt%. At 1.5 Ru wt%, negligible CO_2 slip was maintained with an approximately 20% loss in capture capacity. These results identify Ru-Na/AC as a promising DFM combining high CO_2 uptake, negligible CO_2 slip and cyclic stability. Carbon support played here a dual role: it enabled to study the effect of the alkali metal identity and eliminated the CO_2 slip, which was associated inherently to other reactive oxidic support.

Acknowledgements

Financial support from MICIU/AEI/10.13039/501100011033 and from FEDER, UE through project PID2023-146481OB-I00, and from the Gobierno de Aragón (Grupo Reconocido DGA T03_23R), is gratefully acknowledged. Authors acknowledge the ICTS-CNME and its staff for providing access to their instruments and for their support with the analysis. J.M.C. acknowledges financial support from the PTA2022-022315-I grant, funded by MCIU/AEI/10.13039/501100011033 and by the FSE+.

References

[1] E.T.C. Vogt, B.M. Weckhuysen, The refinery of the future, Nature 629 (2024) 295–306. https://doi.org/10.1038/s41586-024-07322-2.
[2] N. Mac Dowell, P.S. Fennell, N. Shah, G.C. Maitland, The role of CO2 capture and utilization in mitigating climate change, Nature Climate Change 7 (2017) 243–249. https://doi.org/10.1038/nclimate3231.
[3] A. Samanta, A. Zhao, G.K.H. Shimizu, P. Sarkar, R. Gupta, Post-Combustion CO2 Capture Using Solid Sorbents: A Review, Industrial & Engineering Chemistry Research 51 (2011) 1438–1463. https://doi.org/10.1021/ie200686q.
[4] F. Clayer, C.B. Gundersen, M. Norling, L. Pozzoli, A.S. Gragne, T.F. Berglen, Safeguarding drinking water in north-western europe by modelling the fate of amines from CO2 capture, Energy Environ. Sci. 19 (2026) 2922–2937. https://doi.org/10.1039/D5EE07330H.
[5] S.C. Lee, Y.M. Kwon, C.Y. Ryu, H.J. Chae, D. Ragupathy, S.Y. Jung, J.B. Lee, C.K. Ryu, J.C. Kim, Development of new alumina-modified sorbents for CO2 sorption and regeneration at temperatures below 200°C, Fuel 90 (2011) 1465–1470. https://doi.org/10.1016/j.fuel.2010.11.006.

[6] L. Li, B. Zhang, F. Wang, N. Zhao, F. Xiao, W. Wei, Y. Sun, Study of the Novel KMgAl Sorbents for CO2 Capture, Energy Fuels 27 (2013) 5388–5396. https://doi.org/10.1021/ef4010412.
[7] C.J. Keturakis, F. Ni, M. Spicer, M.G. Beaver, H.S. Caram, I.E. Wachs, Monitoring Solid Oxide CO2 Capture Sorbents in Action, ChemSusChem 7 (2014) 3459–3466. https://doi.org/10.1002/cssc.201402474.
[8] S. Jo, H.D. Son, T.-Y. Kim, J.H. Woo, D.Y. Ryu, J.C. Kim, S.C. Lee, K.L. Gilliard-AbdulAziz, Ru/K2CO3–MgO catalytic sorbent for integrated CO2 capture and methanation at low temperatures, Chemical Engineering Journal 469 (2023) 143772. https://doi.org/10.1016/j.cej.2023.143772.
[9] N.N.A.H. Meis, A.M. Frey, J.H. Bitter, K.P. de Jong, Carbon Nanofiber-Supported K2CO3 as an Efficient Low-Temperature Regenerable CO2 Sorbent for Post-Combustion Capture, Ind. Eng. Chem. Res. 52 (2013) 12812–12818. https://doi.org/10.1021/ie4017072.
[10] V.S. Derevschikov, J.V. Veselovskaya, T.Yu. Kardash, D.A. Trubitsyn, A.G. Okunev, Direct CO2 capture from ambient air using K2CO3/Y2O3 composite sorbent, Fuel 127 (2014) 212–218. https://doi.org/10.1016/j.fuel.2013.09.060.
[11] N. Masoud, V. Clement, T. van Haasterecht, M. Führer, J.P. Hofmann, J.H. Bitter, Shedding Light on Solid Sorbents: Evaluation of Supported Potassium Carbonate Particle Size and Its Effect on CO2 Capture from Air, Ind. Eng. Chem. Res. 61 (2022) 14211–14221. https://doi.org/10.1021/acs.iecr.2c01508.
[12] N. Masoud, G. Bordanaba-Florit, T. van Haasterecht, J.H. Bitter, Effect of Support Surface Properties on CO2 Capture from Air by Carbon-Supported Potassium Carbonate, Ind. Eng. Chem. Res. 60 (2021) 13749–13755. https://doi.org/10.1021/acs.iecr.1c01229.
[13] A. Jayakumar, A. Gomez, N. Mahinpey, Kinetic Behavior of Solid K2CO3 under Postcombustion CO2 Capture Conditions, Ind. Eng. Chem. Res. 56 (2017) 853–863. https://doi.org/10.1021/acs.iecr.6b04498.
[14] R.E. Siegel, S. Pattanayak, L.A. Berben, Reactive Capture of CO2: Opportunities and Challenges, ACS Catal. 13 (2023) 766–784. https://doi.org/10.1021/acscatal.2c05019.
[15] J.M. Crawford, M.J. Rasmussen, W.W. McNeary, S. Halingstad, S.C. Hayden, N.S. Dutta, S.H. Pang, Matthew M. Yung, High Selectivity Reactive Carbon Dioxide Capture over Zeolite Dual-Functional Materials, ACS Catal. 14 (2024) 8541–8548. https://doi.org/10.1021/acscatal.4c01340.
[16] M.C. Freyman, Z. Huang, D. Ravikumar, E.B. Duoss, Y. Li, S.E. Baker, S.H. Pang, J.A. Schaidle, Reactive CO2 capture: A path forward for process integration in carbon management, Joule 7 (2023) 631–651. https://doi.org/10.1016/j.joule.2023.03.013.
[17] M.S. Duyar, M.A.A. Treviño, R.J. Farrauto, Dual function materials for CO2 capture and conversion using renewable H2, Applied Catalysis B: Environmental 168–169 (2015) 370–376. https://doi.org/10.1016/j.apcatb.2014.12.025.
[18] L.-P. Merkouri, A.I. Paksoy, T. Ramirez Reina, M.S. Duyar, The Need for Flexible Chemical Synthesis and How Dual-Function Materials Can Pave the Way, ACS Catal. 13 (2023) 7230–7242. https://doi.org/10.1021/acscatal.3c00880.
[19] F. Kosaka, Y. Liu, S.-Y. Chen, T. Mochizuki, H. Takagi, A. Urakawa, K. Kuramoto, Enhanced Activity of Integrated CO2 Capture and Reduction to CH4 under Pressurized Conditions toward Atmospheric CO2 Utilization, ACS Sustainable Chem. Eng. 9 (2021) 3452–3463. https://doi.org/10.1021/acssuschemeng.0c07162.
[20] A. Bermejo-López, B. Pereda-Ayo, J.A. González-Marcos, J.R. González-Velasco, Mechanism of the CO2 storage and in situ hydrogenation to CH4. Temperature and adsorbent loading effects over Ru-CaO/Al2O3 and Ru-Na2CO3/Al2O3 catalysts, Applied Catalysis B: Environmental 256 (2019) 117845. https://doi.org/10.1016/j.apcatb.2019.117845.
[21] S. Cimino, E.M. Cepollaro, L. Lisi, Sulfur tolerance and self-regeneration mechanism of Na-Ru/Al2O3 dual function material during the cyclic CO2 capture and catalytic methanation,

Applied Catalysis B: Environmental 317 (2022) 121705. https://doi.org/10.1016/j.apcatb.2022.121705.
[22] L. Li, S. Miyazaki, S. Yasumura, K.W. Ting, T. Toyao, Z. Maeno, K. Shimizu, Continuous CO2 Capture and Selective Hydrogenation to CO over Na-Promoted Pt Nanoparticles on Al2O3, ACS Catal. (2022) 2639–2650. https://doi.org/10.1021/acscatal.1c05339.
[23] S. Miyazaki, A. Anzai, K. Nagai, T. Miyakage, K. Oguri, S. Mine, T. Toyao, Y. Kanda, N. Maeda, D.M. Meier, K. Shimizu, Continuous CO2 Capture and Selective Reduction to CO over Main-Group Dual-Functional Materials, J. Am. Chem. Soc. (2026). https://doi.org/10.1021/jacs.5c20974.
[24] C. Jeong-Potter, M. Abdallah, C. Sanderson, M. Goldman, R. Gupta, R. Farrauto, Dual function materials (Ru+Na2O/Al2O3) for direct air capture of CO2 and in situ catalytic methanation: The impact of realistic ambient conditions, Applied Catalysis B: Environment and Energy 307 (2022) 120990. https://doi.org/10.1016/j.apcatb.2021.120990.
[25] M. Abdallah, Y. (Iris) Lin, R. Farrauto, Laboratory aging of a dual function material (DFM) washcoated monolith for varying ambient direct air capture of CO2 and in situ catalytic conversion to CH4, Applied Catalysis B: Environmental 339 (2023) 123105. https://doi.org/10.1016/j.apcatb.2023.123105.
[26] Y. (Iris) Lin, M.J. Abdallah, J.E. Peters, T. Luo, H. Sheng, Y.L. Chen, R.J. Farrauto, Aging studies of Dual functional materials for CO2 direct air capture with in situ methanation under simulated ambient conditions: Ru thrifting for cost reduction, Chemical Engineering Journal 479 (2024) 147495. https://doi.org/10.1016/j.cej.2023.147495.
[27] D.Y. Kim, K.-H. Ryu, J. Kang, H.W. Choi, H. Min, Y.J. Kim, P.W. Park, S.B. Kang, Synergistic interaction between Ni and K2CO3 on γ-Al2O3 for integrated direct CO2 capture and methanation under varying humidity conditions, Chemical Engineering Journal 519 (2025) 165593. https://doi.org/10.1016/j.cej.2025.165593.
[28] C. Jeong-Potter, R. Farrauto, Feasibility Study of Combining Direct Air Capture of CO2 and Methanation at Isothermal Conditions with Dual Function Materials, Applied Catalysis B: Environmental 282 (2021) 119416. https://doi.org/10.1016/j.apcatb.2020.119416.
[29] T. Tatsumichi, R. Okuno, H. Hashimoto, N. Namiki, Z. Maeno, Direct capture of low-concentration CO2 and selective hydrogenation to CH4 over Al2O3-supported Ni–La dual functional materials, Green Chem. 26 (2024) 10842–10850. https://doi.org/10.1039/D4GC03218G.
[30] W.W. McNeary, N.C. Ellebracht, M.L. Jue, M.J. Rasmussen, J.M. Crawford, M.M. Yung, A.T. To, S.H. Pang, Application of Solid-Supported Amines for Thermocatalytic Reactive CO2 Capture, ACS Omega 10 (2025) 2364–2371. https://doi.org/10.1021/acsomega.4c10049.
[31] J. Moral-Pombo, E. García-Bordejé, Y. Liu, A. Guerrero-Ruiz, I. Rodríguez-Ramos, CO2 capture from air and its conversion to CH4 using dual functional materials supported on high surface area graphite, Journal of CO2 Utilization 93 (2025) 103054. https://doi.org/10.1016/j.jcou.2025.103054.
[32] E. García-Bordejé, J.M. Conesa, A. Guerrero-Ruiz, I. Rodríguez-Ramos, Integrated CO2 capture from air with unprecedently efficient conversion to methane using Ru-alkali/alumina dual functional material by optimizing alkali loading, Applied Catalysis B: Environment and Energy 385 (2026) 126291. https://doi.org/10.1016/j.apcatb.2025.126291.
[33] E. García-Bordejé, J.M. Conesa, A. Guerrero-Ruiz, I. Rodríguez-Ramos, Bifunctional Na–Ru on gamma-alumina for CO2 capture from air and conversion to CH4: impact of the regeneration method and support on monolithic contactors, Ind. Chem. Mater. 4 (2026) 93–104. https://doi.org/10.1039/D5IM00030K.
[34] F. Karaçoban, Y. Bonne, T. van Haasterecht, J.H. Bitter, On the synergy between Ru and K2CO3 supported on carbon nanofibers for the direct air capture and conversion of CO2, Journal of CO2 Utilization 97 (2025) 103122. https://doi.org/10.1016/j.jcou.2025.103122.

[35] F. Karaçoban, A. Beauvois, J.J. Delgado, L. Gros, G. Li, T. van Haasterecht, J.H. Bitter, Mechanistic understanding of the direct air capture and conversion of CO2 using Ru-K2CO3 based dual functional materials, Applied Catalysis B: Environment and Energy 394 (2026) 126850. https://doi.org/10.1016/j.apcatb.2026.126850.
[36] R.V. Siriwardane, J.M. Cook, Interactions of SO2 with sodium deposited on CaO, Journal of Colloid and Interface Science 114 (1986) 525–535. https://doi.org/10.1016/0021-9797(86)90438-8.
[37] A. Barrie, F.J. Street, An Auger and X-ray photoelectron spectroscopic study of sodium metal and sodium oxide, Journal of Electron Spectroscopy and Related Phenomena 7 (1975) 1–31. https://doi.org/10.1016/0368-2048(75)80052-1.
[38] P.H. Citrin, High-Resolution X-Ray Photoemission from Sodium Metal and Its Hydroxide, Phys. Rev. B 8 (1973) 5545–5556. https://doi.org/10.1103/PhysRevB.8.5545.
[39] L. Giordano, H. Du, V. Castaing, F. Luan, D. Guo, B. Viana, Enhanced red-UC luminescence through Ce3+ co-doping in NaBiF4:Yb3+/Ho3+(Er3+)/Ce3+ phosphors prepared by ultrafast coprecipitation approach, Optical Materials: X 16 (2022) 100199. https://doi.org/10.1016/j.omx.2022.100199.
[40] (n.d.). https://www.harwellxps.guru/xpskb/sodium/#1755794593447-3ccf5452-aec1.
[41] S. Armenise, L. Roldán, Y. Marco, A. Monzón, E. García-Bordejé, Elucidation of Catalyst Support Effect for NH3 Decomposition Using Ru Nanoparticles on Nitrogen-Functionalized Carbon Nanofiber Monoliths, J. Phys. Chem. C 116 (2012) 26385–26395. https://doi.org/10.1021/jp308985x.
[42] S. Sapru, K.D. Hart, C. Zhou, G. Liccardo, J. Oh, M.J. Hollobaugh, J. Osio-Norgaard, A. Majumdar, B.D. Chandler, M. Cargnello, Long-Range Metal–Sorbent Interactions Determine CO2 Capture and Conversion in Dual-Function Materials, ACS Nano 19 (2025) 2484–2496. https://doi.org/10.1021/acsnano.4c13606.
[43] M. Tayyab, V. Natasya, J.-M. Ha, H. Lee, C.-J. Yoo, S. Jin, Direct air capture and isothermal conversion of CO2 to CO over La-based perovskite mixed metal oxides, Applied Catalysis B: Environment and Energy 388 (2026) 126575. https://doi.org/10.1016/j.apcatb.2026.126575.
[44] I. Martínez-López, I. Martín-García, A. Davó-Quiñonero, R. Rodríguez-Bobada, E. Vilaplana-Ortego, E. Guillen-Bas, D. Lozano-Castelló, A. Bueno-López, Fuel from air: NiO-CeO2 nanoparticles, MgO and beta zeolite dual function materials for direct CO2 capture and hydrogenation to CH4, Fuel 398 (2025) 135549. https://doi.org/10.1016/j.fuel.2025.135549.
[45] X. Lin, S. Kim, M. Abdallah, R.J. Farrauto, Enhancement of CO2 adsorption on dual functional materials/catalytic methanation with varying moisture contents present in atmospheric ambient air, Applied Catalysis A: General 709 (2026) 120659. https://doi.org/10.1016/j.apcata.2025.120659.
[46] M. Zhang, Y. Wang, Y. Xu, R. Ma, Q. Shao, B. Xie, X. Zhu, Unraveling the interplay of adsorption and catalytic sites in Ru-Na/Al2O3 for integrated humid direct air capture and methanation, Separation and Purification Technology 394 (2026) 137399. https://doi.org/10.1016/j.seppur.2026.137399.
[47] X. Wu, R. Pandey, R. Krishnamoorti, P. Bollini, Kinetically Constrained Capture and Conversion of CO2 from Ambient Air Using Excess Oxygen-Derived Recalcitrant Carbonates, ACS Catal. (2026). https://doi.org/10.1021/acscatal.5c08102.
[48] J. Feng, Y. Zhang, L. Li, S. Zhao, W. Qiu, J. Lu, Y. Ning, Z. Huang, H. Lin, A novel NiCa-based dual-functional material with high absorption capacity and stability for integrated direct air CO2 capture and in-situ methanation, Separation and Purification Technology 354 (2025) 128989. https://doi.org/10.1016/j.seppur.2024.128989.
[49] J. Lee, J. Otomo, Low-Temperature Activated Direct Air Capture Methanation Using K-β" Alumina, Ind. Eng. Chem. Res. 62 (2023) 12096–12108. https://doi.org/10.1021/acs.iecr.3c00828.

Supplementary Files

This is a list of supplementary files associated with this preprint. Click to download.

- SUPPLEMENTARYINFORMATIONARTICLEONCARBONMATERIALS260916.docx